Green Chemistry

Accepted Manuscript

ROYAL SOCIETY OF CHEMISTRY

www.rsc.org/greenchem

Cotton derived porous carbon via an MgO template method for high performance lithium ion battery anode

Chunyu Zhu[a]*, Tomohiro Akiyama[a]

[a]Center for Advanced Research of Energy & Materials, Hokkaido University, Sapporo 060-8628, Japan

*Corresponding author: Tel.: +81-11-706-6842; Fax: +81-11-726-0731.

E-mail address: chunyu6zhu@gmail.com or chunyu6zhu@eng.hokudai.ac.jp (Chunyu Zhu)

Abstract

Porous carbon has received great attentions for electrochemical energy storage devices. In this study, we proposed a novel and scalable method to fabricate porous carbon, which contained macro and mesopores, from sustainable biomass raw material of cotton cellulose. MgO template, which acted as pore creator, was incorporated into the cellulose-derived carbon by absorbing a $Mg(NO_3)_2$ solution in cellulose fibers with subsequent drying and carbonization processes. After removing the MgO template by acid leaching, porous carbon was produced with a specific surface area as high as 1260 m^2 g^{-1}. The sample showed attractive electrochemical performances as the anode material for Li ion batteries (LIBs). The carbon anode delivered a high reversible capacity of 793 mAh g^{-1} at a current density of 0.5 A g^{-1} after 500 cycles. The carbon anode also showed a high-rate capability, and a capacity of 355 mAh g^{-1} can be obtained at a current density of 4 A g^{-1}. A wide comparison with literatures also showed that the cotton-derived porous carbon was among the most promising carbon-based anodes for LIBs.

Keywords: Li ion battery, anode, carbon, cotton, cellulose

1. Introduction

To meet the increasing demands for mobile electronics and electric vehicles, significant attention has been paid to develop high capacity electrode materials for lithium-ion batteries (LIBs).[1, 2] Many novel anode materials have been explored for higher specific capacity and better cycling performance, such as carbonaceous materials,[3-5] silicon,[6, 7] tin,[8, 9] metal oxides,[10-15] and so on. Among them, carbonaceous materials have demonstrated to be the most promising and common anode materials for LIBs.[16-18] Although graphite has been widely used as an anode material in current commercial LIBs because of its low cost and low electrochemical potential with respect to lithium metal, its low theoretical capacity (372 mAh g^{-1}) and poor rate capability cannot meet the increasing requirements for the next-generation LIBs with high energy and high power densities. Therefore, great efforts have been made to explore novel carbon materials possessing high capacity, high rate capability, and easy accessibility. Many novel carbon anodes, including carbon nanofibers,[19-21] carbon nanotubes (CNTs),[22] graphenes,[3, 23] and porous carbons[5, 24-26] have been investigated. For electrochemical applications, materials with porous structure such as porous oxide LIB cathode materials, [27-30] porous oxide LIB anode materials, [9, 31, 32] and porous carbons, [5, 20, 25, 26, 33] can provide shortened mass diffusion distances and high contact areas between the solid and electrolyte, which results in enhanced performance. Many methods have been used to prepare porous carbon materials, such as silica template method,[34, 35] spray pyrolysis,[36] electrospinning-carbonization using precursors of melamine and polyacrylonitrile,[21] ice-templating-carbonization of polyacrylonitrile precursor,[25] and so on. However, most of the synthesis methods require special equipments, high-cost reagents or complex process control. Recently, the use of biomasses to produce carbon materials has received tremendous attentions because of the abundant raw materials and low cost. Many studies have been engaged with the production of carbonaceous materials for LIB anodes from biomasses such as bacterial cellulose,

[20] cornstalk waste,[4] ox horns,[5] corn starch,[26] sweet potato,[37] lignin, [38] banana peels,[39] bamboo chopsticks, [40] and so on. However, the reported electrochemical performance is still limited. Cotton is one of the most abundant, sustainable and environmentally friendly biomass materials in nature, which contains 90–95% cellulose, making it a promising raw material for the fabrication of carbon. Several groups have reported the production of porous carbon fibers with high specific surface area from cotton as effective sorbents for waste water cleanup and electrochemical supercapacitor.[41-45] The cellulose-derived carbon materials, which used bamboo chopsticks [40] and bacterial cellulose [20] as raw materials, have been evaluated as LIB anodes. Nevertheless, a relatively low capacity was still delivered in such an electrode material. Herein, we report a facile and scalable strategy to prepare highly porous carbon using cotton cellulose as raw material. MgO template is incorporated into the cellulose-derived carbon, which acts as pore creator, by absorbing a $Mg(NO_3)_2$ solution in cellulose fibers with subsequent drying and carbonization processes. After the removal of MgO template by acid leaching, highly porous carbon can be obtained, which possesses high specific surface area and macro/mesopores. When evaluated as the anode material for LIBs, the sample exhibits attractive electrochemical performances.

2. Experimental section

2.1 Material preparation: In the experiment, magnesium nitrate of 5, 10, 15, and 20 mmol were dissolved in 10 ml of distilled water to form homogenous solutions, respectively. The above solutions were immerged with 1.5 g commercially available dewaxed cotton, respectively. After that, the wet cottons absorbed with the above solutions were dried at 60 ^{o}C overnight. The dried samples were annealed at 800 ^{o}C for 2 h at a heating rate of 10 ^{o}C min^{-1} under Ar flow. Subsequently, the annealed samples were pulverized using a mortar-pestle for 10 min. Finally, the pulverized samples were leached with 0.2 M HCl for 24 h, washed with distilled water and ethanol for several times, and dried at 100 ^{o}C under vacuum overnight. As a comparison, dewaxed cotton without the immersion of magnesium nitrate was also annealed at the same condition. These samples were named as Mg0, Mg5, Mg10, Mg15, and Mg20, respectively, based on the amount of magnesium nitrate. Additionally, the Mg15 samples annealed at 700 and 900 ^{o}C were also obtained to evaluate the effect of calcination temperature on the electrochemical properties.

2.2 Material characterization: The samples were analyzed by X-ray diffraction (XRD, Rigaku Miniflex, CuKα), scanning electron microscopy (SEM, JEOL, JSM-7400F), and transmission electron microscopy (TEM, 200 kV, JEM-2010F) for their crystalline structure and morphology characterizations. An X-ray energy dispersive spectrometer (EDS) under SEM environment was used for elemental analysis. Raman spectra of the samples were acquired from a RENISHAW Raman spectrometer using an excitation wavelength of 532 nm. The Brunauer–Emmett–Teller (BET) specific surface area of the as-synthesized samples was measured using a Quantachrome surface area analysis instrument by N_2 absorption–desorption. The pore size distributions were determined using the density functional theory (DFT) method.

***2.3 Electrochemical measurement*:** A two-electrode Swagelok cell was used for the

electrochemical test. The working electrode consisted of the active material, acetylene black conductive carbon, and polyvinylidene fluoride (PVDF) binder in a weight ratio of 75:10:15. A lithium disk was used as the reference and counter electrode, and a 1 M solution of $LiPF_6$ dissolved in a 50:50 (v/v) mixture of ethylene carbonate (EC) and dimethyl carbonate (DMC) was used as the electrolyte. Cell assembly was carried out in an Ar-filled glove-box. Galvanostatic discharge/charge measurement was performed using an Arbin battery tester in a potential range of 3.0 and 0.01 V versus Li/Li^+ at a constant temperature of 25 ºC. A potentiostat/galvanostat apparatus (Autolab, PGSTAT128N) was employed for cyclic voltammetry (CV) measurement at a potential scanning rate of 0.1 mV s^{-1} in a voltage range of 0-3.0 V.

3. Results and discussion

The structure and morphology properties of the samples were first studied by XRD, Raman, and SEM. Figure S1 (Electronic Supplementary Information, ESI) shows the SEM images of the original cotton fibers and the fibers after absorption of $Mg(NO_3)_2$. The cotton fibers have diameter of several microns and length in millimeter order. It is noted that $Mg(NO_3)_2$ precursor is homogenously immersed into the cotton fibers, and a morphology difference is not observed for the fibers before and after the absorption of $Mg(NO_3)_2$. Figure S2 (ESI) presents the XRD patterns of the samples after heat treatment at 800 ^oC for 2 h under Ar flow. The peaks of these patterns can be indexed to a single phase of MgO (PDF No. 00-004-0829). The $Mg(NO_3)_2$ precursor as-immersed in cotton fibers was decomposed into MgO, accompanying with the pyrolysis of cellulose to form carbon. Carbon peaks were not observed due to its low crystallinity. The MgO peak intensity for these samples increases in a sequence of increasing amount of $Mg(NO_3)_2$ precursor. Figure S3 (ESI) shows the SEM images of the MgO/carbon composites, which were obtained after heat treatment. Samples Mg5 and Mg10 exhibit macroporous fibers with length of several tens of microns. The samples are greatly pulverized for Mg15 and Mg20, and it is difficult to find an entire fiber. Figure S4 (ESI) illustrates the EDS spectra of the MgO/carbon composites, and the samples show increasing intensity of Mg and O peaks as the increase of MgO contents. The MgO phase can be easily removed by acid leaching. Figure S5 (ESI) shows a typical EDS spectrum of the sample after acid leaching and the peak representing Mg element disappear, indicating the successful removal of MgO. Figure 1 (a) exhibits the XRD patterns of the obtained samples after heat treatment at 800 ^oC and being leached with HCl solution. Two peaks located at 23.6 ° and 43.6 ° can be assigned to the (002) and (100) reflections of graphitic carbon, respectively. These peaks are greatly broadened and weak, indicating the amorphous feature of the synthesized carbon. In Figure 1 (b), Raman

spectra show typical characteristic D-band (defective and disordered carbon) and G-band (graphitic carbon) of carbon, located at around 1335 and 1600 cm^{-1}, respectively. The intensity ratio of the D-band to G-band (ID/IG) for sample Mg0 is approximately 0.8, while the ratios for samples Mg5, Mg10, Mg15 and Mg20 are approximately 0.9. The relative high values of ID/IG indicate the disordering of the obtained carbon samples, agreeing with the XRD results.

SEM images of the carbon samples are shown in Figure 2. The sample Mg0, as-derived from the directly pyrolyzed cotton fibers, consists of fibers with various lengths and irregular particles. This is because of that the originally long fibers after pyrolysis were pulverized before use. Not an image of highly porous structure is confirmed for this sample. This is the biggest difference to the MgO-templated samples. SEM observation clearly demonstrates that the MgO-templated samples possess macropores of several hundreds of nanometers. The samples become much more pulverized as the increase of MgO amount. For the sample Mg20, it is even difficult to find a fiber shape.

The morphology and structural observation was further investigated using TEM, as shown in Figure 3. Figure 3 (a) shows a typical TEM image at a low magnification. It is confirmed that the templated carbon possesses a porous structure with interconnected pores of several hundreds of nanometers. Inset presents the typical selected area electron diffraction of the carbon material, which indicates a typical graphite structure. Figures 3 (b, c) illustrates the high-resolution TEM image. The sample is highly defective although some distorted lattice fringes corresponding to the graphitic (002) plane can be seen.

The specific surface area and pore size distribution of the carbon materials were measured by nitrogen absorption-desorption experiment. Nitrogen sorption isotherms and pore size distribution of the carbon samples are presented in Figure 4. The specific surface areas of the samples were evaluated by BET method, and the values are 115, 1012, 1100, 1260, and 1104 m^2

g^{-1} for samples Mg0, Mg5, Mg10, Mg15, and Mg20, respectively. Pore size distributions of the MgO-template samples were estimated by the density functional theory, and the samples show mesopores concentrated at approximately 3–5 nm.

The electrochemical properties of the porous carbon anodes were analyzed by CV tests and galvanostatic discharge/charge measurements. Figure 5 presents the CV curves of sample Mg0 (a) and sample Mg15 (b) in a potential range of 3.0–0 V for the initial four cycles. The shape of the CV curves for samples Mg5, Mg10, and Mg20 are similar to that of sample Mg15, as shown in Figure S6 (ESI). In the first cathodic scans, the apparent areas centered at ~0.6 V are observed for all samples, which radically drop from the second cycle. This is associated with the irreversible capacities caused by the decomposition of electrolyte and the formation of solid-electrolyte interface (SEI) layer.[20, 36, 37] The CV curves nearly overlap after the first cycle, implying the excellent reversibility and stability of the porous carbon for Li insertion and extration. It is noted that the MgO-templated carbon electrodes show much larger covered areas than the non-template carbon, indicating higher Li storage capacity for the MgO-template samples.

Figure 6 displays the galvanostatic discharge/charge cycling performance over the voltage range of 3.0–0.01 V. All electrodes were firstly cycled at a current density of 0.5 A g^{-1} to 500 cycles, after which the samples Mg10, Mg15, and Mg20 continued to be cycled to 800 cycles at increasing current densities of 1.0 and 2.0 A g^{-1}. Figure 6 (a) presents the reversible discharge/charge capacities versus cycling number. It can be clearly seen that all samples exhibit excellent cycling stability, and the reversible capacities of the samples have a decreasing sequence of Mg15, Mg10, Mg20, Mg5, and Mg0. Sample Mg15 demonstrates the highest capacity during the 500 cycles at a current density of 0.5 A g^{-1}, and a high value of 793 mAh g^{-1} is obtained after 500 cycles. As a comparison, the reversible capacities after 500 cycles for

samples Mg0, Mg5, Mg10, and Mg20 are 289, 382, 653, and 657 mAh g^{-1}, respectively. At increased current densities to 1.0 and 2.0 A g^{-1}, sample Mg15 demonstrates high reversible capacities of above 595 and 447 mAh g^{-1}, respectively, which are higher values than those for samples Mg10 and Mg20. It is noted that, after 800 cycles, sample Mg15 still presents a higher reversible capacity of 447 mAh g^{-1} at 2.0 A g^{-1}. Figures 6 (b, c, d) shows the typical discharge/charge profiles for these samples. In the first cycles, the samples Mg0, Mg5, Mg10, Mg15, and Mg20 deliver discharge/charge capacities of 541.71/298.44, 1250.12/534.21, 1979.92/926.19, 2291.07/1052.76, and 1683.49/775.39 mAh g^{-1} at 0.5 A g^{-1}, respectively. The capacities for the MgO-template samples are greatly higher than that of the commercial graphite with a theoretical capacity of 372 mAh g^{-1}. An obvious plateau at around 0.7 V is observed in the first discharge curves for all samples, corresponding to the additional peaks in the CV curves, which cover the irreversible part of initial discharge capacity. This is caused by the decomposition of electrolyte and the formation of SEI layer. The calculated initial Coulombic efficiency for lithium extraction-to-insertion for these sample are 55.09%, 42.73%, 46.78%, 45.95%, and 46.06%, respectively, which are similar values as the reported carbon anodes.[3, 5, 20, 26, 34, 46] However, from the second cycle, the discharge plateaus at 0.7 V disappear, and the discharge curves show continuous potential decrease from 1.5 V to 0.01 V as the proceeding of lithium insertion into carbon materials. The Coulombic efficiencies for the samples were increased to ~90% in the second cycle, and were quickly improved to > 97% after a few cycles, as shown in Figure S7 (ESI).

The above samples were obtained by heat treatment at 800 ^{o}C. The samples Mg15 annealed at 700 and 900 ^{o}C were also obtained, and the galvanostatic discharge/charge cycling performance is shown in Figure S8. It is observed that the sample annealed at 800 ^{o}C exhibits the highest capacity.

The rate performance of the best carbon electrode for sample Mg15 annealed at 800 ^{o}C was further studied, as shown Figure 7. Reversible capacities of around 1020, 815, 715, 625, 500, 405, 355 mAh g^{-1} can be obtained at gradually increasing current densities of 0.25, 0.5, 0.75, 1, 2, 3, and 4 A g^{-1}, respectively. After 125 cycles, the current density was further decreased to 1 and 0.5 A g^{-1}, and surprisingly, high capacities of around 675 and 820 mAh g^{-1} can be recovered. When the electrode was continued to be cycled to 400 cycles at 2 A g^{-1}, a high capacity of around 510 mAh g^{-1} was obtained. The electrode presents Coulombic efficiency higher than 97% after the initial several cycles.

SEM images of sample Mg15 after cycling were also obtained, as shown in Figure S9. It is observed that the cycled electrode is covered with a dense SEI layer, however, the morphology of carbon barely change. The similar morphology indicates perfect structural stability during the Li insertion/extraction processes.

The above results demonstrate that the cotton-derived porous carbon is an excellent electrode material for high power and high energy LIBs with good cyclability. The superior electrochemical performance can be explained by its novel nanostructure. First, the high specific surface area of the porous carbon with interconnected macropores and mesopores provide efficient access of electrolyte to the electrode surface and facilitate fast charge transfer, leading to lower transport resistance and higher electrochemical activity. Second, the functional pores with different dimensions may act as reservoirs for the storage of Li ions. Third, the 3D porous network structure is mechanically strong to accommodate the volume change caused by repeated Li insertion/extraction during cycling.

The electrochemical performance of the porous carbon is also comparable to that of the frontier carbon-based anode material as reported. Table 1 shows a comparison of the performance of the cotton-derived porous carbon with the state-of-the-art carbon materials,

including the sweet potato-derived carbon nanoparticles[37], porous carbon nanofiber webs derived from bacterial cellulose[20], porous carbon nanofibers/nanosheets hybrid from cornstalk waste[4], N-rich porous carbon derived from ox horns[5], microsized porous carbon spheres from corn starch[26], electrospun carbon nanofibers[19, 21], pseudographite from banana peels[39], carbon fibers from bamboo chopsticks[40], and N-rich porous carbon spheres by SiO_2 template method[34]. Notably, the cotton-derived porous carbon displays the best performance among these carbon materials, especially the long-cycling and high-rate performance.

Table 1. Comparison of cycling and rate performance of the carbon anode of present work and the reported carbon anodes.

Sample	Cyclability	Rate performance
This work: cellulose-derived porous carbon by a MgO-template method	0.5 A g^{-1}, 500 cycle, 793 mAh g^{-1}; 2 A g^{-1}, 800 cycle, 447 mAh g^{-1}	1020 mAh g^{-1} at 0.25 A g^{-1}; 815 mAh g^{-1} at 0.5 A g^{-1}; 715 mAh g^{-1} at 0.75 A g^{-1}; 625 mAh g^{-1} at 1 A g^{-1}; 500 mAh g^{-1} at 2 A g^{-1}; 405 mAh g^{-1} at 3 A g^{-1}; 355 mAh g^{-1} at 4 A g^{-1}
R1: Sweet potato-derived carbon nanoparticles [37]	0.1 A g^{-1}, 200 cycle, 320 mAh g^{-1};	285 mAh g^{-1} at 0.186 A g^{-1}; 235 mAh g^{-1} at 0.372 A g^{-1}; 126 mAh g^{-1} at 1.86 A g^{-1}; 84 mAh g^{-1} at 3.72 A g^{-1}
R2: Porous carbon nanofiber webs derived from bacterial cellulose [20]	0.1 A g^{-1}, 100 cycle, 914 mAh g^{-1}; 0.3 A g^{-1}, 100 cycle, 713 mAh g^{-1}; 1 A g^{-1}, 100 cycle, 549 mAh g^{-1}; 2 A g^{-1}, 100 cycle, 414 mAh g^{-1};	1068 mAh g^{-1} at 0.1 A g^{-1}; 769 mAh g^{-1} at 0.3 A g^{-1}; 608 mAh g^{-1} at 0.6 A g^{-1}; 505 mAh g^{-1} at 1.0 A g^{-1}; 436 mAh g^{-1} at 2 A g^{-1}; 334 mAh g^{-1} at 4 A g^{-1}; 261 mAh g^{-1} at 8 A g^{-1}; 250 mAh g^{-1} at 10 A g^{-1}
R3: Porous carbon nanofibers/ nanosheets hybrid from cornstalk waste [4]	0.1 A g^{-1}, 200 cycle, 592 mAh g^{-1}	578 mAh g^{-1} at 0.1 A g^{-1}; 553 mAh g^{-1} at 0.3 A g^{-1}; 527 mAh g^{-1} at 0.6 A g^{-1}; 508 mAh g^{-1} at 1.0 A g^{-1}; 474 mAh g^{-1} at 2.0 A g^{-1}; 454 mAh g^{-1} at 3.0 A g^{-1}
R4: N-rich porous carbon derived from ox horns [5]	0.1 A g^{-1}, 100 cycle, 1178 mAh g^{-1} 1.0 A g^{-1}, 100 cycle, 591 mAh g^{-1}	1181 mAh g^{-1} at 0.1 A g^{-1}; 1031 mAh g^{-1} at 0.2 A g^{-1}; 898 mAh g^{-1} at 0.3 A g^{-1}; 808 mAh g^{-1} at 0.4 A g^{-1}; 750 mAh g^{-1} at 0.5 A g^{-1}; 592 mAh g^{-1} at 1.0 A g^{-1}; 470 mAh g^{-1} at 2.0 A g^{-1}; 304 mAh g^{-1} at 5 A g^{-1}
R5: micro-sized porous carbon spheres from corn starch [26]	0.1 A g^{-1}, 100 cycle, 507 mAh g^{-1}	400 mAh g^{-1} at 0.2 A g^{-1}; 340 mAh g^{-1} at 0.5 A g^{-1}; 305 mAh g^{-1} at 1 A g^{-1}; 280 mAh g^{-1} at 2 A g^{-1}; 245 mAh g^{-1} at 5 A g^{-1}
R6: Electrospun carbon nanofibers with Fe catalyst [19]	1 A g^{-1}, 100 cycle, 609 mAhg^{-1}	983 mAh g^{-1} at 0.1A g^{-1}; 318 mAh g^{-1} at 3 A g^{-1}
R7: N-enriched porous carbon nanofiber networks by electrospinning [21]	0.05 A g^{-1}, 50 cycle, 1150 mAhg^{-1}	1315 mAh g^{-1} at 0.05 A g^{-1}; 1145 mAh g^{-1} at 0.1 A g^{-1}; 906 mAh g^{-1} at 0.2 A g^{-1}; 654 mAh g^{-1} at 0.5 A g^{-1}; 473 mAh g^{-1} at 1 A g^{-1};
R8: Pseudographite from banana peel [39]	0.1 A g^{-1}, 11 cycle, 790 mAh g^{-1}; 0.1 A g^{-1}, 300 cycle, 717 mAhg^{-1}	738 mAh g^{-1} at 0.2 A g^{-1}; 634 mAh g^{-1} at 0.5 A g^{-1}; 518 mAh g^{-1} at 1 A g^{-1}; 385 mAh g^{-1} at 2 A g^{-1}; 243 mAh g^{-1} at 5 A g^{-1}
R9: N-rich porous carbon spheres by SiO_2 template method [34]	0.5 A g^{-1}, 100 cycle, 540 mAh g^{-1};	542 mAh g^{-1} at 0.5 A g^{-1}; 410 mAh g^{-1} at 1 A g^{-1}; 293 mAh g^{-1} at 2 A g^{-1}; 215 mAh g^{-1} at 3 A g^{-1};
R10: Carbon fibers from bamboo chopsticks [40]	0.137 A g^{-1}, 800 cycle, 360 mAh g^{-1}	353 mA h g^{-1} at 0.17 A g^{-1}; 319 mA h g^{-1} at 0.342 A g^{-1}; 292 mA h g^{-1} at 0.517 A g^{-1}; 254 mA h g^{-1} at 1.03 A g^{-1}; 211 mA h g^{-1} at 2.06 A g^{-1}; 137 mAh g^{-1} at 4.59 A g^{-1}

4. Conclusions

In summary, we have demonstrated a facile and scalable method to fabricate porous carbon, with high specific surface area (1260 $m^2 g^{-1}$) and interconnected macro/mesopores, from a low-cost, eco-friendly and scalable biomass raw material of cotton cellulose. In the synthesis, MgO-template was introduced to the cellulose-derived carbon, which acted as pore creator, by absorbing a $Mg(NO_3)_2$ solution in cellulose fibers with subsequent drying and carbonization processes. As an anode material for LIBs, the porous carbon anode delivered a high reversible capacity of 793 mAh g^{-1} at a current density of 0.5 A g^{-1} after 500 cycles. The carbon anode also showed a high-rate capability, and a capacity of 355 mAh g^{-1} was obtained at a current density of 4 A g^{-1}. The greatly improved electrochemical performance can be attributed to its porous structural features, which can enlarge the mass-electrolyte contact area, shorten the lithium ion diffusion length, and accommodate volume expansion during lithiation reaction. Given the abundant and renewable resource of cellulose, the as-prepared porous carbon can satisfy the increasing demand of anode materials for LIBs.

Acknowledgements

This work was financially supported partially by the Japan Society for Promotion of Science (JSPS) and Yashima Environment Technology Foundation. The authors would like to thank Dr. G. Saito for his support on TEM observation.

References

1. D. Larcher and J. M. Tarascon, *Nat Chem*, 2015, 7, 19-29.
2. M. M. Thackeray, C. Wolverton and E. D. Isaacs, *Energy & Environmental Science*, 2012, 5, 7854-7863.
3. Y. Xu, Z. Lin, X. Zhong, B. Papandrea, Y. Huang and X. Duan, *Angewandte Chemie*, 2015, 127, 5435-5440.
4. S. Wang, C. Xiao, Y. Xing, H. Xu and S. Zhang, *Journal of Materials Chemistry A*, 2015, 3, 6742-6746.
5. J. Ou, Y. Zhang, L. Chen, Q. Zhao, Y. Meng, Y. Guo and D. Xiao, *Journal of Materials Chemistry A*, 2015, 3, 6534-6541.
6. N. Liu, Z. Lu, J. Zhao, M. T. McDowell, H.-W. Lee, W. Zhao and Y. Cui, *Nat Nano*, 2014, 9, 187-192.
7. X. Liu, Y. Gao, R. Jin, H. Luo, P. Peng and Y. Liu, *Nano Energy*, 2014, 4, 31-38.
8. G. Saito, C. Zhu and T. Akiyama, *Advanced Powder Technology*, 2014, 25, 728-732.
9. L. Zhang, H. B. Wu, B. Liu and X. W. Lou, *Energy & Environmental Science*, 2014, 7, 1013-1017.
10. C. Zhu, N. Sheng and T. Akiyama, *RSC Advances*, 2015, 5, 21066-21073.
11. X. Zhu, G. Ning, X. Ma, Z. Fan, C. Xu, J. Gao, C. Xu and F. Wei, *Journal of Materials Chemistry A*, 2013, 1, 14023-14030.
12. Y. Deng, L. Wan, Y. Xie, X. Qin and G. Chen, *RSC Advances*, 2014, 4, 23914-23935.
13. M. V. Reddy, G. V. Subba Rao and B. V. R. Chowdari, *Chemical Reviews*, 2013, 113, 5364-5457.
14. C. Zhu, G. Saito and T. Akiyama, *Journal of Alloys and Compounds*, 2015, 646, 639-646.
15. C. Zhu, G. Saito and T. Akiyama, *Journal of Alloys and Compounds*, 2015, 633, 424-429.
16. C. Zhang, W. Lv, Y. Tao and Q.-H. Yang, *Energy & Environmental Science*, 2015, 8, 1390-1403.
17. A. D. Roberts, X. Li and H. Zhang, *Chemical Society Reviews*, 2014, 43, 4341-4356.
18. S. Dutta, A. Bhaumik and K. C. W. Wu, *Energy & Environmental Science*, 2014, 7, 3574-3592.
19. B. Zhang, Z.-L. Xu, Y.-B. He, S. Abouali, M. Akbari Garakani, E. Kamali Heidari, F. Kang and J.-K. Kim, *Nano Energy*, 2014, 4, 88-96.
20. W. Wang, Y. Sun, B. Liu, S. Wang and M. Cao, *Carbon*, 2015, 91, 56-65.
21. D. Nan, Z.-H. Huang, R. Lv, L. Yang, J.-G. Wang, W. Shen, Y. Lin, X. Yu, L. Ye, H. Sun and F. Kang, *Journal of Materials Chemistry A*, 2014, 2, 19678-19684.

22. R. A. DiLeo, A. Castiglia, M. J. Ganter, R. E. Rogers, C. D. Cress, R. P. Raffaelle and B. J. Landi, *ACS Nano*, 2010, 4, 6121-6131.
23. Z. Jiang, B. Pei and A. Manthiram, *Journal of Materials Chemistry A*, 2013, 1, 7775-7781.
24. Y. Fang, Y. Lv, R. Che, H. Wu, X. Zhang, D. Gu, G. Zheng and D. Zhao, *Journal of the American Chemical Society*, 2013, 135, 1524-1530.
25. A. D. Roberts, S. Wang, X. Li and H. Zhang, *Journal of Materials Chemistry A*, 2014, 2, 17787-17796.
26. M. Chen, C. Yu, S. Liu, X. Fan, C. Zhao, X. Zhang and J. Qiu, *Nanoscale*, 2015, 7, 1791-1795.
27. L. Zhou, D. Zhao and X. Lou, *Angewandte Chemie International Edition*, 2012, 51, 239-241.
28. C. Zhu and T. Akiyama, *RSC Advances*, 2014, 4, 10151-10156.
29. C. Zhu, G. Saito and T. Akiyama, *Journal of Materials Chemistry A*, 2013, 1, 7077-7082.
30. F. Cheng, H. Wang, Z. Zhu, Y. Wang, T. Zhang, Z. Tao and J. Chen, *Energy & Environmental Science*, 2011, 4, 3668-3675.
31. D. Cai, D. Wang, H. Huang, X. Duan, B. Liu, L. Wang, Y. Liu, Q. Li and T. Wang, *Journal of Materials Chemistry A*, 2015, 3, 11430-11436.
32. S. Guo, G. Lu, S. Qiu, J. Liu, X. Wang, C. He, H. Wei, X. Yan and Z. Guo, *Nano Energy*, 2014, 9, 41-49.
33. X. He, X. Peng, Y. Zhu, C. Lai, C. Ducati and R. V. Kumar, *Green Chemistry*, 2015, 17, 4637-4646.
34. D. Li, L.-X. Ding, H. Chen, S. Wang, Z. Li, M. Zhu and H. Wang, *Journal of Materials Chemistry A*, 2014, 2, 16617-16622.
35. D.-C. Guo, F. Han and A.-H. Lu, *Chemistry – A European Journal*, 2015, 21, 1520-1525.
36. V. Etacheri, C. Wang, M. J. O'Connell, C. K. Chan and V. G. Pol, *Journal of Materials Chemistry A*, 2015, 3, 9861-9868.
37. P. Zheng, T. Liu, J. Zhang, L. Zhang, Y. Liu, J. Huang and S. Guo, *RSC Advances*, 2015, 5, 40737-40741.
38. W. E. Tenhaeff, O. Rios, K. More and M. A. McGuire, *Advanced Functional Materials*, 2014, 24, 86-94.
39. E. M. Lotfabad, J. Ding, K. Cui, A. Kohandehghan, W. P. Kalisvaart, M. Hazelton and D. Mitlin, *ACS Nano*, 2014, 8, 7115-7129.
40. J. Jiang, J. Zhu, W. Ai, Z. Fan, X. Shen, C. Zou, J. Liu, H. Zhang and T. Yu, *Energy &*

Environmental Science, 2014, 7, 2670-2679.

41. H. Bi, X. Huang, X. Wu, X. Cao, C. Tan, Z. Yin, X. Lu, L. Sun and H. Zhang, *Small*, 2014, 10, 3544-3550.
42. B. Wang, R. Karthikeyan, X.-Y. Lu, J. Xuan and M. K. H. Leung, *Industrial & Engineering Chemistry Research*, 2013, 52, 18251-18261.
43. H. Bi, Z. Yin, X. Cao, X. Xie, C. Tan, X. Huang, B. Chen, F. Chen, Q. Yang, X. Bu, X. Lu, L. Sun and H. Zhang, *Advanced Materials*, 2013, 25, 5916-5921.
44. W. Shen, T. Hu, P. Wang, H. Sun and W. Fan, *ChemPlusChem*, 2014, 79, 284-289.
45. G. Ma, D. Guo, K. Sun, H. Peng, Q. Yang, X. Zhou, X. Zhao and Z. Lei, *RSC Advances*, 2015, 5, 64704-64710.
46. M. Ashokkumar, N. T. Narayanan, A. L. Mohana Reddy, B. K. Gupta, B. Chandrasekaran, S. Talapatra, P. M. Ajayan and P. Thanikaivelan, *Green Chemistry*, 2012, 14, 1689-1695.

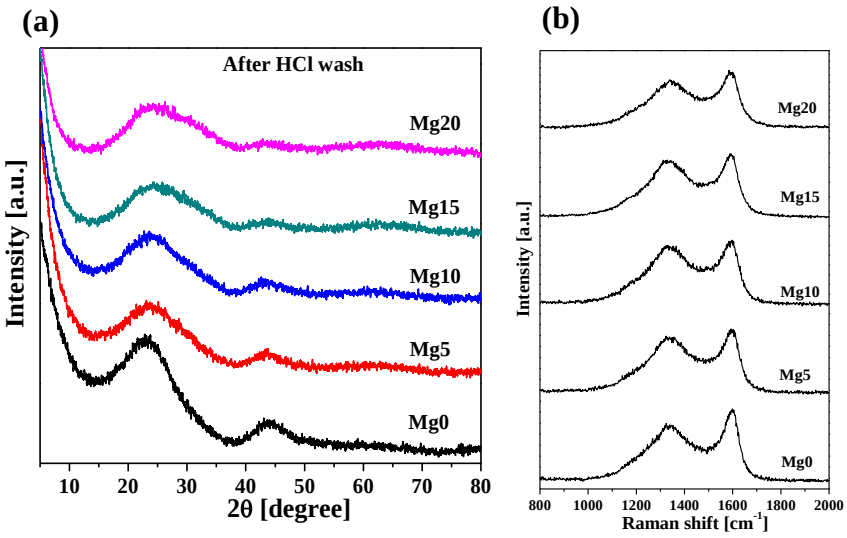

Figure 1. XRD patterns (a) and Raman spectra (b) of the synthesized samples.

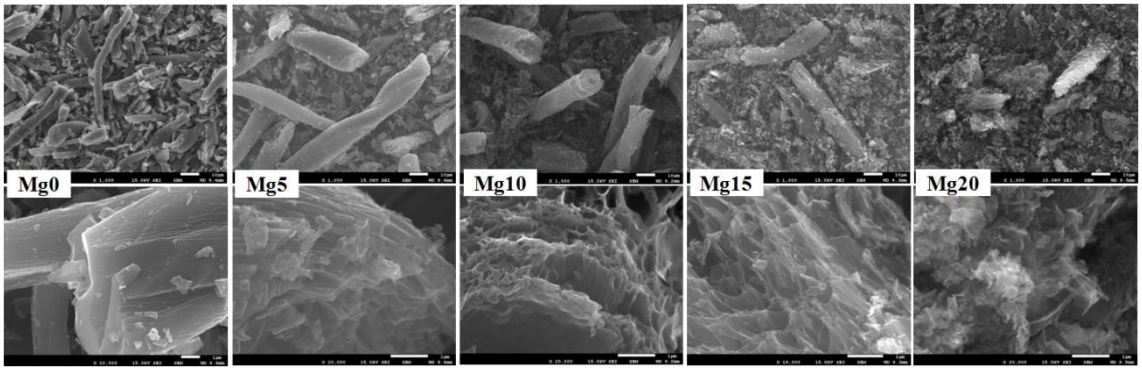

Figure 2. SEM images of the synthesized samples.

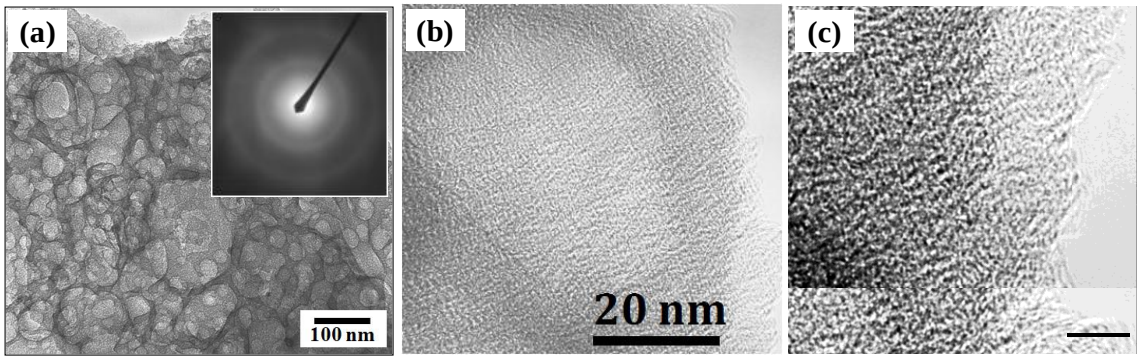

Figure 3. TEM (a) and high-resolution TEM images (b, c) for sample Mg15.

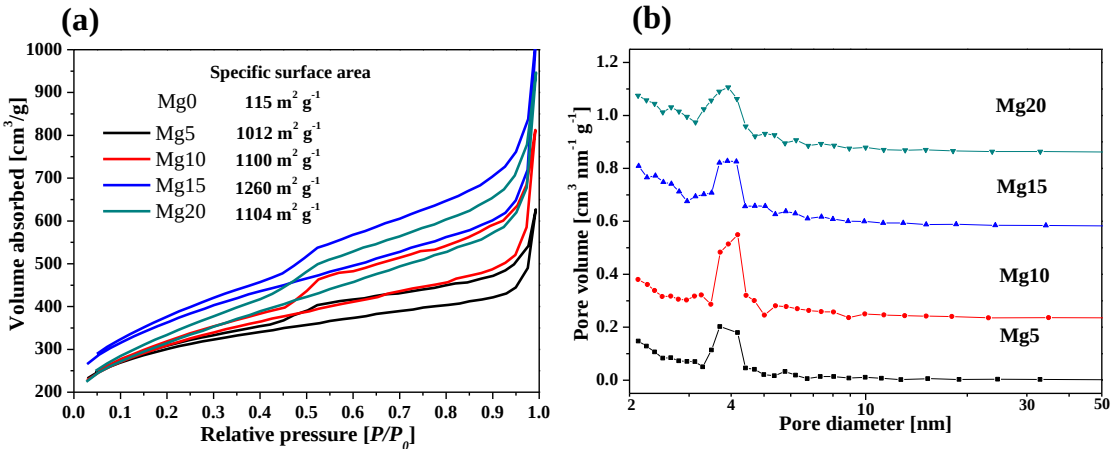

Figure 4. N_2 absorption-desorption isotherms (a) and pore size distribution (b) of the synthesized samples.

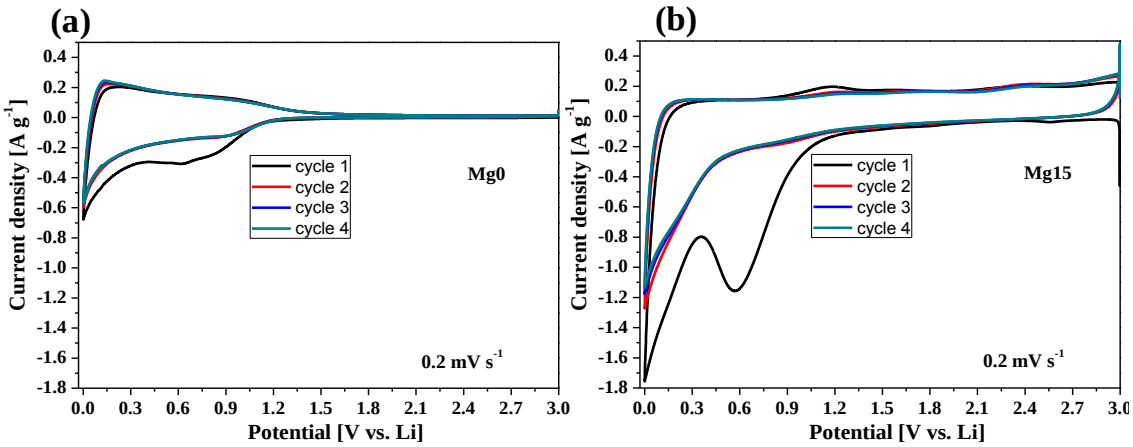

Figure 5. Representative CV curves of samples Mg0 (a) and Mg15 (b). The curves for samples Mg5, Mg10, and Mg20 are shown in Figure S6.

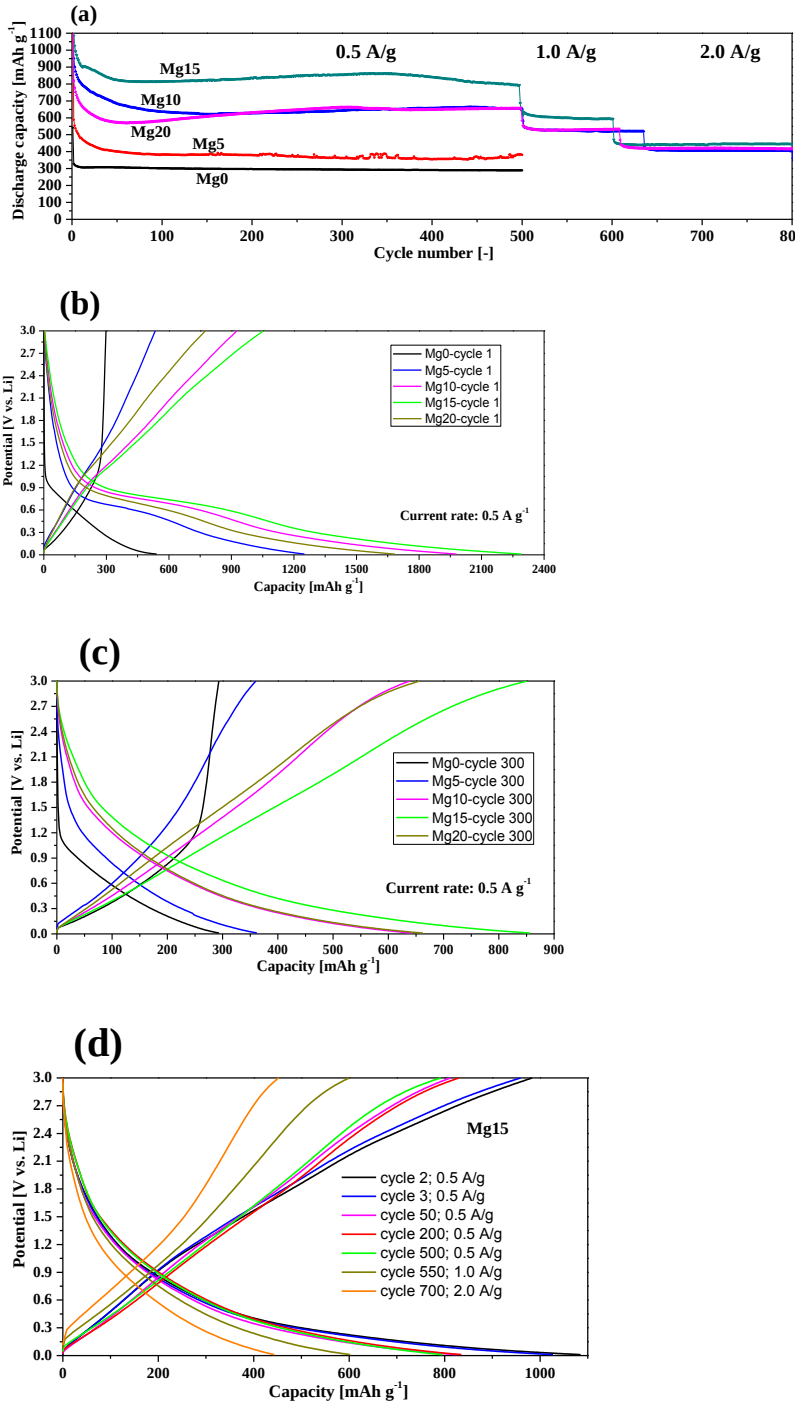

Figure 6. (a) Cycling performance of the synthesized carbon samples. (b, c, d) Galvanostatic charge-discharge profiles.

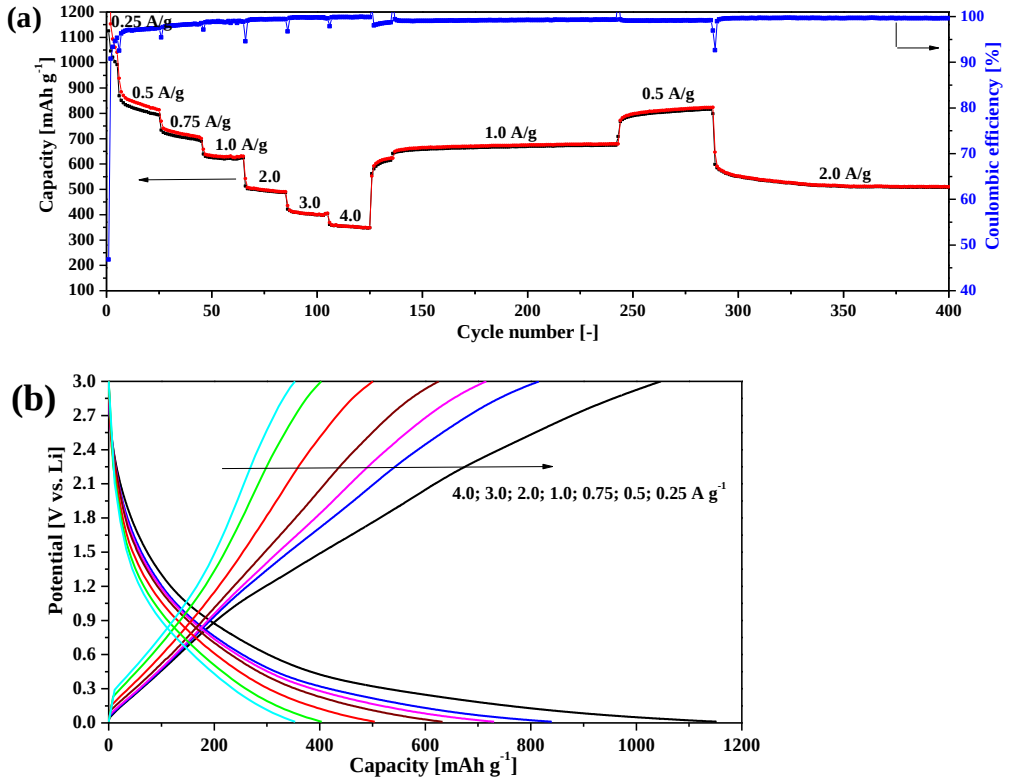

Figure 7. (a) Rate capabilities and cycle performance of sample Mg15 cycled at different current rates. (b) Galvanostatic charge-discharge profiles of sample Mg15 at different current rates.

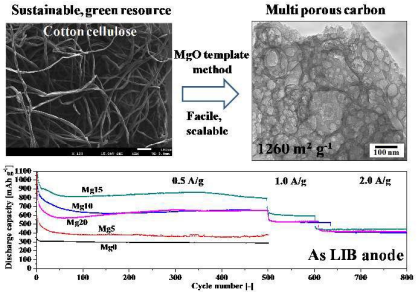

This paper presents a biomass-derived porous carbon containing macro/mesopores for high-performance LIB anodes.